Tuning of the Mechanical Properties of a Laser Powder Bed Fused Eutectic High Entropy Alloy $Ni_{30}Co_{30}Cr_{10}Fe_{10}Al_{18}W_2$ through Heat Treatment

Yiwei Yu[a], Yakai Zhao[b], Kai Feng[a,*], Rong Chen[d], Bolun Han[a], Kaifeng Ji[a], Meng Qin[a], Zhuguo Li[a,*], Upadrasta Ramamurty[b,c]

[a]Shanghai Key Laboratory of Materials Laser Processing and Modification, School of Materials Science and Engineering, Shanghai Jiao Tong University, Shanghai 200240, China

[b]Institute of Materials Research and Engineering (IMRE), Agency for Science, Technology and Research (A*STAR), Singapore 138634, Republic of Singapore

[c]School of Mechanical and Aerospace Engineering, Nanyang Technological University, Singapore 639798, Republic of Singapore

[d]School of Mechanical Engineering and Electronic Information, China University of Geosciences, Wuhan 430074, China

[*]Corresponding authors; e-mail: fengkai@sjtu.edu.cn; lizg@sjtu.edu.cn

Abstract: Eutectic high entropy alloys (EHEA) with an exceptional combination of strength and ductility are promising candidates as advanced structural materials. However, achieving an optimal balance between the properties in additively manufactured EHEAs is an outstanding challenge. In this work, $Ni_{30}Co_{30}Cr_{10}Fe_{10}Al_{18}W_2$ EHEA was additively manufactured using the laser powder bed fusion (LPBF) technique. In the as-fabricated state, it exhibits a dual-phase nano-lamellar structure consisting of FCC/$L1_2$ and B2 phases. Post-fabrication heat treatments were explored for modulating microstructure and, in turn, enhancing the mechanical properties, so as to achieve an optimum balance between strength and ductility. Upon heat treatment at 750 °C for 1 h, part of the B2 phase transformed into FCC, with the appearance of the tungsten-rich precipitates inside the B2 phase. The average interlayer spacing of the FCC/$L1_2$ lamellae increased to 124 nm, while that of B2 lamellae decreased to 86 nm, resulting in an alloy with an ultimate tensile strength (UTS) of 1811 MPa, although the strain to failure (ε_f) decreased to 2%. Upon increasing

the heat treatment temperature to 1000 °C, the average interlayer spacings of the FCC and B2 phases increased to 210 and 187 nm, respectively, which resulted in a more balanced mechanical behavior with UTS and ε_f of 1332 MPa and 9.3%, respectively. This study provides an effective approach for microstructural modulation and enhancement of mechanical properties of LPBF fabricated EHEA via post-fabrication heat treatment, offering insights for developing future high-performance alloys for advanced structural applications.

Keywords: Eutectic high entropy alloys, LPBF, phase modulation, mechanical properties, post heat treatment

1. Introduction

The demand for high-performance alloys for structural applications in the aerospace, automotive, and energy industries is perennial [1]. However, conventional approaches in alloy design can no longer meet the requirements for the fast iterations in complex and high-performance materials development. In this context, a novel alloy design concept, high entropy alloy (HEA), which was initially proposed by Yeh et al. [2] and Cantor et al. [3] and involves five or more elements in approximately equal atomic ratios, attracted considerable attention. Due to their unique composition and microstructures, HEAs can offer exceptional properties such as high fracture toughness [4-6], good oxidation resistance [7, 8], outstanding corrosion and hydrogen embrittlement resistances [9-12], and superior irradiation resistance [13, 14].

While single-phase HEAs with the face centered cubic (FCC) crystal structure exhibit superior plasticity [15], it comes at the cost of strength. In contrast, single-phase body centered cubic (BCC) HEAs offer high strength but are limited in terms of ductility [16]. Achieving an optimum combination of high strength and ductility in an alloy with a single solid solution phase remains a key problem in achieving high performance HEAs. To address the conflict between the strength and ductility, Lu et al. [17] developed eutectic high entropy alloys (EHEA). The $AlCoCrFeNi_{2.1}$ EHEA that involves both the FCC/$L1_2$ phase and B2/BCC phase provides an alternative in balancing strength and ductility. Subsequently, hypoeutectic $AlCoCrFeNi_{2.0}$ and hypereutectic $AlCoCrFeNi_{2.2}$ have been developed, which demonstrate exceptional strength and ductility [18].

The microstructure evolution involving elemental segregation, precipitate formation and phase transformation in HEAs is highly dependent on the cooling rate during the manufacturing process [19, 20]. The solidification rates in conventional approaches used for the HEA fabrication, including arc-melting [21], vacuum induction melting [22, 23], and spark plasma sintering [24], are typically less than 100 K/s [25]. Strikingly, laser powder bed fusion (LPBF), a widely studied additive manufacturing technology, can provide a high cooling rate that ranges between 10^4 and 10^6 K/s [26, 27]. Prior works on the LPBF $AlCoCrFeNi_{2.1}$ EHEA show an ultrafine-grained microstructure in it, compared to that in the as-cast sample, implying strong grain refinement during the rapid solidification intrinsic to the LPBF process [28]. Lan et al. [29] found that the average grain size in the XZ plane of as-built sample decreases with an increase in the volumetric energy density (VED). Guo et al. [30] observed that the

transition in eutectic morphology from the lamellar to the cellular structure can be enforced by decreasing VED. These studies show that tailoring of the microstructures–and hence mechanical properties–of EHEAs is possible using LPBF [31].

Furthermore, Small amounts of Mo and W can be dissolved in EHEA [32-34], enhancing the lattice distortion that is typical of HEAs, and further increasing the tensile strength to over 1200 MPa [35]. Yang et al. [36] obtained an ultrafine eutectic structure in $Ni_{30}Co_{30}Cr_{10}Fe_{10}Al_{18}W_1Mo_1$ using LPBF with a few alloying additions. The sizes of eutectic lamellae and colonies range from 150–200 nm and 2–6 μm, respectively, leading to an ultimate tensile strength (UTS) of over 1400 MPa at room temperature. For comparison, the as-cast $Ni_{30}Co_{30}Cr_{10}Fe_{10}Al_{18}W_2$ EHEA only has a UTS of 1266.5 MPa [35]. Process optimization and microstructural evolution of as-cast and as-built EHEAs have been widely studied.

However, the rapid cooling rates inherent to LPBF often result in non-equilibrium characteristics that may not always lead to an optimal mechanical performance [37, 38]. As a result, post-fabrication heat treatment becomes crucial for further tuning the microstructure and optimizing the mechanical performance of EHEAs. Heat treatments can induce phase transformations, precipitate formation, and microstructural coarsening, which can be exploited judiciously for balancing strength and ductility [39]. Moreover, heat treatment helps enhance the phase stability, relieve residual stresses, and refine the critical microstructural features such as lamellar spacing, resulting in improved mechanical properties. Previous studies have demonstrated that the post-fabrication heat treatments significantly improve the mechanical performance of HEAs [40, 41].

In this work, a dual-phase nano-lamellar $Ni_{30}Co_{30}Cr_{10}Fe_{10}Al_{18}W_2$ EHEA was fabricated using LPBF. The effects of heat treatment temperatures ranging from 750 to 1000 °C on the microstructures and mechanical properties were systematically investigated. Related microstructural mechanisms such as structural stability, phase transformation, and coarsening have been studied. Precipitation and dissolution behaviors of $L1_2$ precipitates within the FCC phase and W-rich nanoparticles within the B2 phase have been revealed, as well as the consequent hardening and softening phenomena. It thus provides an alternative in the customization of microstructure and mechanical properties of LPBF fabricated EHEAs by post fabrication heat treatment process, which can be promising in high performance EHEAs development.

2. Materials and methods

2.1 Powders

The pre-alloyed powder of $Ni_{30}Co_{30}Cr_{10}Fe_{10}Al_{18}W_2$ EHEA was prepared through vacuum induction gas atomization. Characterization using a MIRA 3 high-resolution scanning electron microscope (SEM, TESCAN, Czech Republic) indicates that the powder has good sphericity with only a few satellite particles attached on the surface (Figure 1a). The particle size distribution was analyzed using a laser particle size analyzer (Microtrac S3500, US) and the results are shown in Figure 1b. The D10, D50, and D90 of the powders are 18.23, 32.31, and 55.71 μm, respectively. An energy dispersive X-ray spectroscopy (EDS) instrument, attached to the SEM, was utilized for elemental mapping of the powder, as shown in Figures 1c and 1d. The elements are found to be uniformly distributed without any obvious macroscopic segregation. The chemical composition (in at.%) of the powder is listed in Table 1.

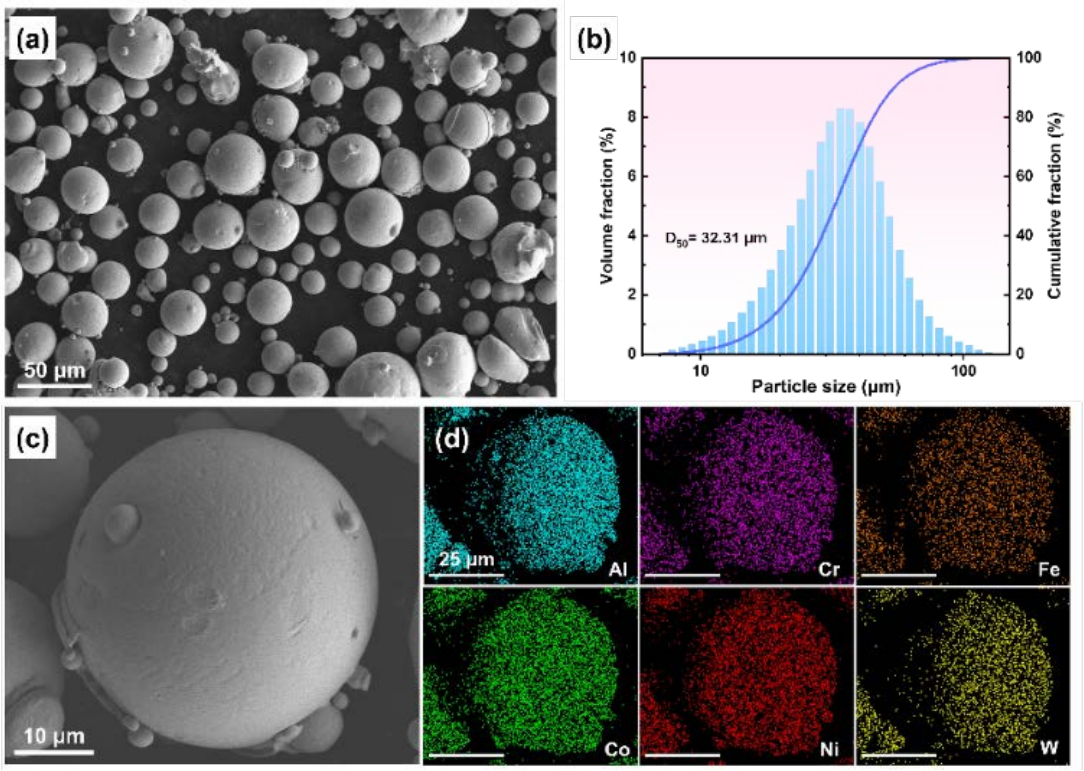


Figure 1 $Ni_{30}Co_{30}Cr_{10}Fe_{10}Al_{18}W_2$ EHEA powder. (a) SEM image, (b) Powder size distribution, (c) SEM image of selected particle, (d) EDS elemental mapping of the particle in (c).

Table 1 Chemical compositions (at.%) of the $Ni_{30}Co_{30}Cr_{10}Fe_{10}Al_{18}W_2$ EHEA powder

Ni	Co	Cr	Fe	Al	W
31.22	30.33	9.84	9.87	16.86	1.89

2.2 Sample preparation

The $Ni_{30}Co_{30}Cr_{10}Fe_{10}Al_{18}W_2$ EHEA samples were fabricated using a TruPrint 1000 3D printer (TRUMPF, Germany), as shown in Figure 2a. The printer is equipped with a Nd: YAG fiber laser, which can generate a maximum laser power of 200 W with a spot diameter of 80 μm. High purity argon gas was used as the protective atmosphere during fabrication to maintain minimum oxygen content (below 200 ppm) inside the printing chamber. A 5×5 mm^2 checkerboard scanning strategy was employed to suppress cracking and reduce stress. An angle of 67° between successive layers was used to control the anisotropy [42], as illustrated in Figure 2b. A polished 316 stainless steel with a diameter of 98 mm was used as the substrate.

The volumetric energy density (VED) has been used as a direct parameter to describe the incident laser energy, which can be calculated as[43]:

$$E = P / (v_s h t) \quad (1)$$

where P is the laser power, v_s is the scanning speed, h represents the hatch spacing, and t is the layer thickness. These parameters determine the solidification conditions during printing and the resulting grain morphology, thus affecting the relative density of the fabricated samples. By conducting the parameters optimization process, the optimal combination (laser power: 120 W, scanning speed: 1100 mm/s, hatch spacing: 0.07 mm, layer thickness: 0.02 mm, VED: 77.92 J/mm^3) was then decided based on the sample having the highest density of 99.73%. These parameters were then used to build samples with dimensions of 30×14×5 mm^3 for subsequent microstructural characterizations and mechanical tests. After printing, the samples were annealed at temperatures of 750, 800, 900, and 1000 °C for 1 h with a heating rate of 20 °C/min, followed by water quenching.

2.3 Microstructural characterization

Phase identification of the specimens was performed using a D8 ADVANCE Da Vinci X-ray diffractometry (XRD, Bruker, Germany), equipped with a Cu target X-ray

source. The diffraction angle range was from 10° to 90° with a scanning speed of 5°/min. XRD was performed on the surface of the sample is normal to the build direction (BD). The morphologies and compositions of the specimens were characterized using SEM equipped with EDS, backscattered electron (BSE), and electron backscatter diffraction (EBSD) detectors. For SEM, specimens were all vibratory-polished to obtain mirror finish of surface and eliminate residual stress from mechanical polishing. For transmission electron microscope (TEM) sample preparation, selected specimens were mechanically polished to a thickness of less than 60 μm and then punched into 3 mm circular discs. The samples were further thinned to approximately 40 nm using ion milling. The microstructures and precipitates were then characterized with a Talos F200X TEM (Thermo Fisher Scientific, USA).

Tensile tests were performed using a servo-hydraulic 810 MTS testing machine (MTS Corp., USA). The tensile strain was measured using an ARAMIS v6.1 digital image correlation (DIC, GOM Optical Tech., Germany). Uniaxial testing was conducted at a strain rate of 10^{-3} s^{-1} at room temperature, with three repeated tests for each condition. The dimensions of the dog-bone-shaped tensile specimens were 24 mm in length, 10 mm in width, and 1 mm in thickness. The gauge length and width are 8 and 2 mm, respectively (Figure 2c). The tensile test direction is normal to BD, as illustrated in Figure 2d.

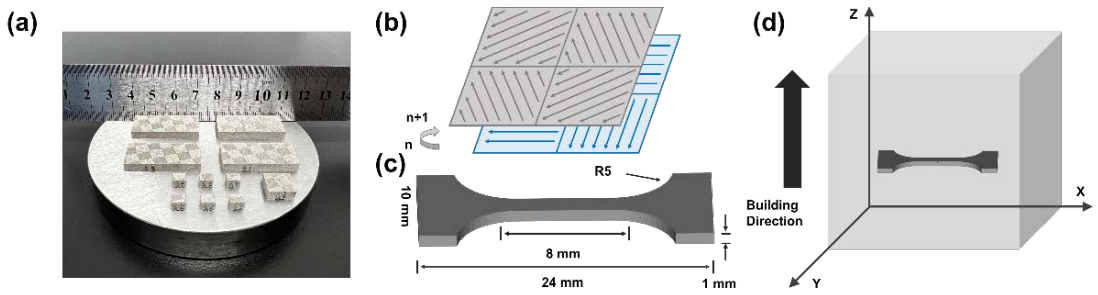


Figure 2 LPBF fabricated EHEA samples. (a) Optical image of the as-built EHEA samples. (b) Schematic of scanning strategy for LPBF. (c) Geometry and dimension of the specimen for tensile test. (d) Schematic illustration of tensile specimen direction with respect to the build direction.

3 Results

3.1 Phase distribution and microstructures

Figure 3a shows the XRD spectra obtained on the pre-alloyed $Ni_{30}Co_{30}Cr_{10}Fe_{10}Al_{18}W_2$ EHEA powder and on the as-built EHEA sample. In both the cases, FCC and BCC dual-phase structures, with intense (111) diffraction peak for the FCC phase and (110) diffraction peak for the BCC phase, were observed [44]. Based on previous reports, the $Ni_{30}Co_{30}Cr_{10}Fe_{10}Al_{18}W_2$ EHEA consists of FCC and B2 phases [35,

[45, 46]. Although it is difficult to judge whether there are ordered $L1_2$ or B2 phases from current XRD, it is still possible that the $L1_2$ precipitates are embedded within the FCC matrices at a nanoscale size [44] and that the BCC phase is a NiAl-type ordered intermetallic (B2). This will be further explored in the subsequent TEM analysis.

The pole figure distributions obtained using EBSD reveal the maximum intensity of multiples of uniform density (MUD) value of 23.02 for the FCC/$L1_2$ phase and 28.28 for the BCC/B2 phase, as shown in Figure 3b. These high MUD values indicate a strong texture in the as-built sample, which can lead to anisotropic tensile properties. The interface between the FCC and BCC phases can also be defined by the Kurdjumov-Sachs (K-S) orientation relationship, specifically $<011>_{FCC/L12}$ // $<111>_{BCC/B2}$ and $\{111\}_{FCC/L12}$ // $\{011\}_{BCC/B2}$. Generally, this specific orientation can be observed in dual-phase steels, which is known to minimize the lattice mismatch and thereby reduce the interfacial energy [47]. Figure 3c further shows the phase map from the side view (surface parallel to BD), where eutectic structures with alternating lamellae of the FCC/$L1_2$ (red, 31.9 vol.%) and BCC/B2 (blue, 68.1 vol.%) phases appear. The yellow line in Fig. 3c indicates the K-S orientation relationship between the two phases. Additionally, the inverse pole figure map shows a preferential growth orientation of <001>//BD for FCC/$L1_2$ and <101>//BD for BCC/B2, which is consistent with the XRD results shown in Figure 3a.

Typical lamellar microstructures with eutectic colonies exhibiting various crystallographic orientations are confirmed along BD. In Figure 3e, the eutectic colonies grow towards the directions perpendicular to the local melt pool boundary, as sketched by the white dashed line, which aligns with the direction of thermal gradient. While the fine lamellae (FCC/$L1_2$ phase, dark in Fig. 3f) and the coarse lamellae (BCC/B2 phase, bright in Fig. 3f) can be observed, it should be noted that such dual-phase lamellar eutectic structures are much finer than those of the as-cast alloy and comparable with the those reported in the LPBF $AlCoCrFeNi_{2.1}$ EHEA [35, 48].

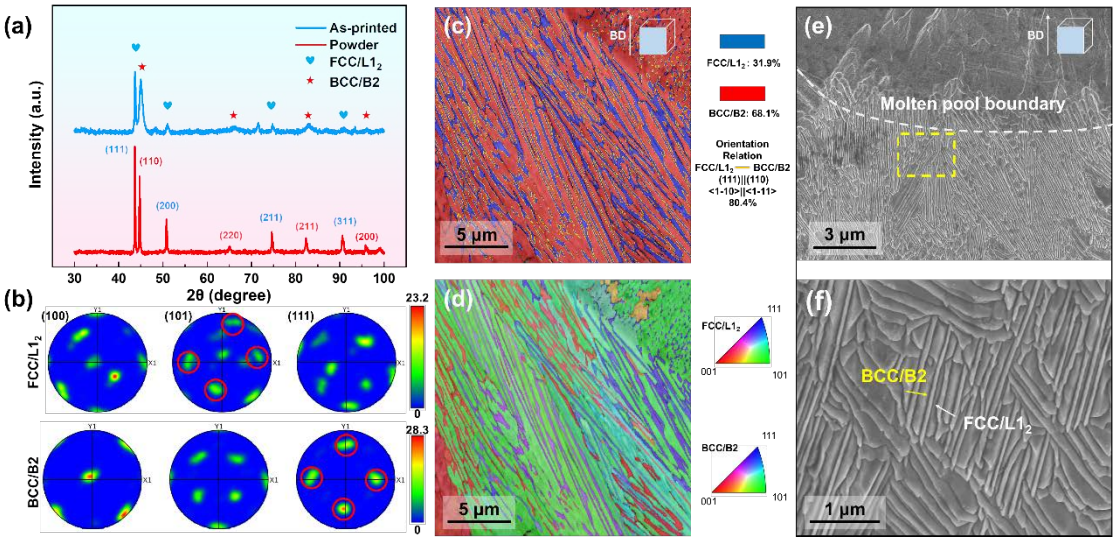


Figure 3 (a) XRD spectra of as-built $Ni_{30}Co_{30}Cr_{10}Fe_{10}Al_{18}W_2$ EHEA sample and the pristine powder. (b) Pole figures of FCC/$L1_2$ and BCC/B2 phases. (c) Phase map and (d) IPF map of as-built EHEA along building direction. (e) SEM image of the cross-section. (f) Magnified SEM image of selected region in (e).

The scanning TEM (STEM) image in Figure 4a shows that the average thicknesses of the FCC and BCC lamellae are around 89 ±17 and 174 ±28 nm, respectively. The K-S orientation relationship can also be verified by the semi-coherent interface and the corresponding selected area electron diffraction (SAED) pattern (upper right of Figure 4a). It is known that the segregation of Fe and W can be relatively weakened due to the high cooling rates (10^4–10^6 K/s) that prevail during the LPBF process [49]. The EDX results indicate that the BCC phase is enriched in Al and Ni but depleted in Co, Cr, and Fe, whereas the FCC phase is enriched in Cr and Co but depleted in Al and Ni (Figures 4b–d). Notably, the SAED pattern demonstrates weak superlattice spots in both FCC and BCC phases. It implies that the FCC phase contains the ordered $L1_2$ phase, and the BCC phase is a NiAl-type ordered intermetallic B2 phase (Figures 4e–f) [46]. Unexpectedly, there is no obvious elemental segregations in the FCC versus $L1_2$ phases, which may be attributed to the rapid cooling rate during the solidification process. The B2 phase, on the other hand, possesses enriched Ni and Al and is a NiAl-type ordered intermetallic [35].

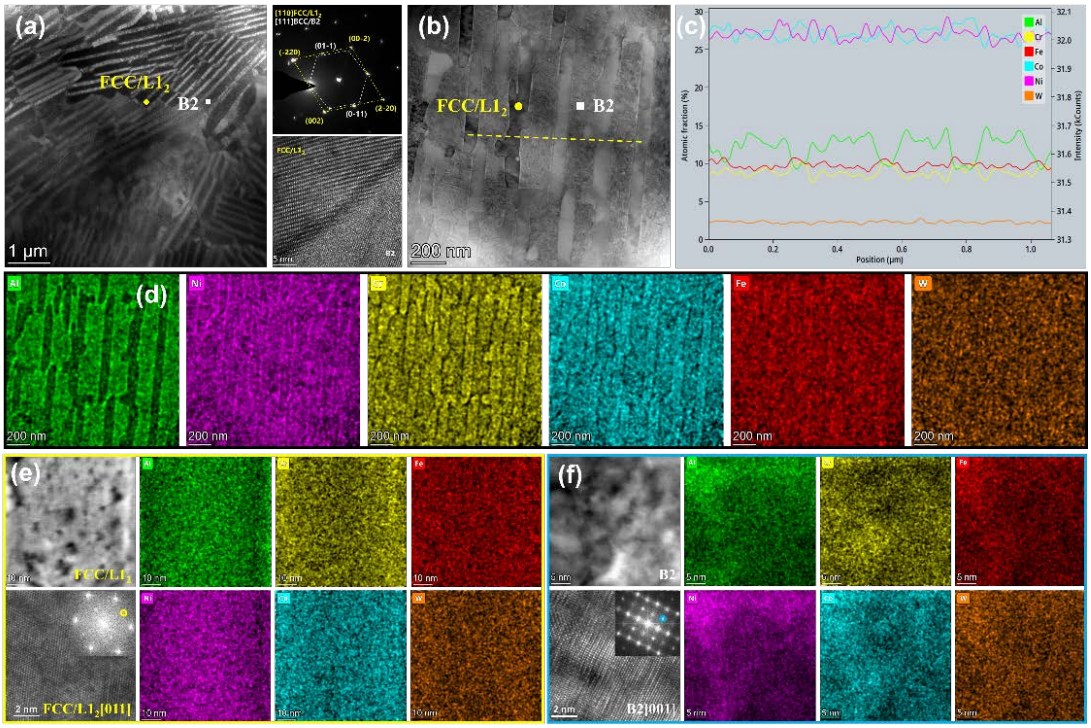


Figure 4 (a) STEM image of as-built $Ni_{30}Co_{30}Cr_{10}Fe_{10}Al_{18}W_2$ EHEA sample and typical semi-coherent interface with the corresponding SAED pattern. (b) TEM image and (c) EDX line scanning of as-built EHEA with mixed phases. (d) EDX elemental mapping of Al, Ni, Co, Cr, Fe, W. (e) Bright field STEM image of FCC/$L1_2$ phase and corresponding EDX elemental mapping. (f) Bright field STEM image of B2 phase and corresponding EDX elemental mapping.

3.2 Effects of heat treatment

It is known that the rapid cooling rate during LPBF process results in the formation of non-equilibrium microstructures. By precisely controlling the heating and cooling processes during heat treatment, uniform and stable microstructures can be expected, thus improving the mechanical performance of the LPBF alloys. Figure 5 shows the XRD spectra of the samples after annealing at 750, 800, 900, and 1000 °C for 1 hour. All the samples exhibit a dual-phase structure consisting of the FCC and B2 phases. Specifically, a noticeable shift to lower angles of the FCC (220) peak after heat-treatment at higher temperatures can be observed, indicating an increase of lattice parameters as well as lattice distortion.

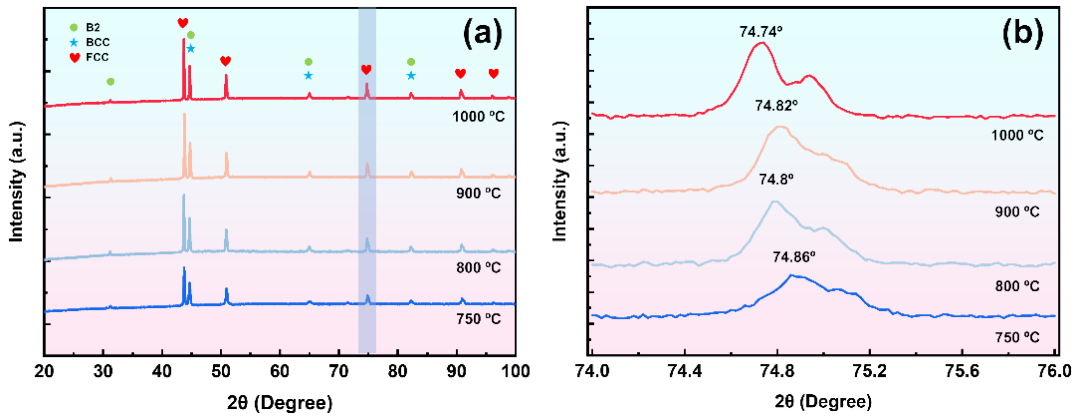


Figure 5 (a) XRD spectra of LPBF fabricated samples after heat treatment at different temperatures. (b) Enlarged XRD spectra at selected position of FCC phase in (a).

Figures 6a_1–d_1 show the BSE images of samples parallel to BD after heat treatment at different temperatures. Alternating lamellar structure with bright (FCC phase) and dark (B2 phase) contrast can be observed. The color differentiation between these two phases is attributed to the variation in elemental distribution. The bright nanoparticles are W-rich precipitates (based on the EDS results). Notably, the ultrafine lamellar structures are almost retained after heat treatment at 750 °C for 1 h, which is similar to those in the as-built sample in Figure 3e. When the annealing temperature is increased to 800 °C, coarsening initiates in both the FCC and B2 phases. A notable microstructure transformation occurs with further coarsening and spheroidization of both phases at 900 °C. The lamellae become highly irregular and dispersed, indicating an increased atomic mobility and element diffusion rate across the phase boundaries at this temperature. When the sample is heat-treated at 1000 °C, equiaxed grains are observed, suggesting a near-equilibrium state. Interestingly, the tungsten-rich precipitates are no longer observed in 1000 °C heat-treated sample.

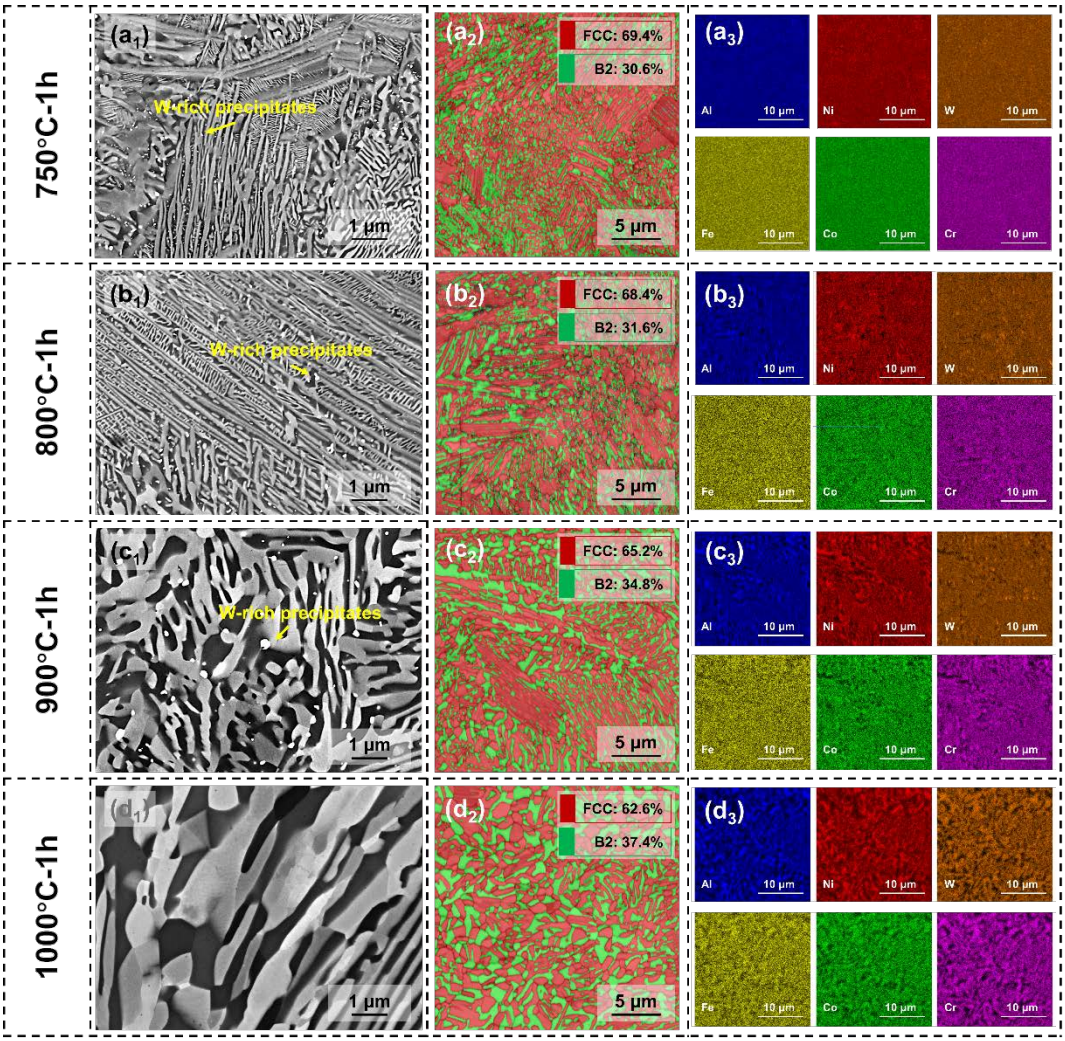


Figure 6 BSE, EBSD, and SEM-EDS images of the as-built samples after heat treatments at different temperatures: (a) 750 °C for 1 h, (b) 800 °C for 1 h, (c) 900 °C for 1 h, (d) 1000 °C for 1 h. Note that the BSE, EBSD, and SEM-EDS images for same smple are not at the same location or magnification.

The EBSD results displayed in Figures 6a_2–d_2 further reveal that the heat-treated $Ni_{30}Co_{30}Cr_{10}Fe_{10}Al_{18}W_2$ EHEA samples consist of FCC and B2 phases. After heat treatment at 750 °C for 1 h, the volume fraction of FCC phase is 69.4%, which is double that in as-built sample (31.9% in Figure 3c), while the volume fraction of B2 phase is 20.6%. Upon increasing the heat treatment temperature to 1000 °C, however, the volume fraction of FCC phase gradually decreases, which is consistent with the result in literature [50]. Based on the EDS elemental mapping results, stronger element segregation occurs in the heat-treated samples at higher temperatures, which can be ascribed to accelerated atomic diffusions at elevated temperatures [50]. Similar to the case of the as-built sample, FCC phase is enriched in Co, Cr, Fe, and W, while the B2 phase is enriched in Al and Ni. Notably, phase transition from FCC to B2 occurs after

heat treatment at 800 °C for 1 h. When the temperature is increased to 1000 °C, phase segregation is enhanced significantly. This indicates that the intense atomic diffusion can significantly promote elemental segregation within the alternating lamellae at elevated temperatures.

3.3 Mechanical properties

The representative engineering stress-strain curves of the as-built and heat-treated samples are presented in Figure 7a. The as-built sample does not show a distinct yield behavior; its UTS and strain to failure (ε_f) are 1549 MPa and 5.2%, respectively. After heat treatment, markedly different mechanical properties are obtained. Specifically, the UTS increases to 1811 MPa after heat treatment at 750 °C for 1 h, though the elongation decreases to 3.2%. When the heat treatment temperature is 800 °C, the alloy achieves a UTS of 1575 MPa with an elongation of 7.35%, indicating simultaneous improvements in both strength and ductility. However, when the heat treatment temperature is above 800 °C, the elongation increases with temperature, while the UTS decreases. Figure 7b shows the Vickers hardness of as-built and heat-treated samples (750-1000 °C) is 454, 626, 477, 431, and 417 HV. The highest hardness is achieved after heat treatment at 750 °C with an increase of 37.9% compared to the as-built sample. The evolution in hardness is consistent with that in UTS.

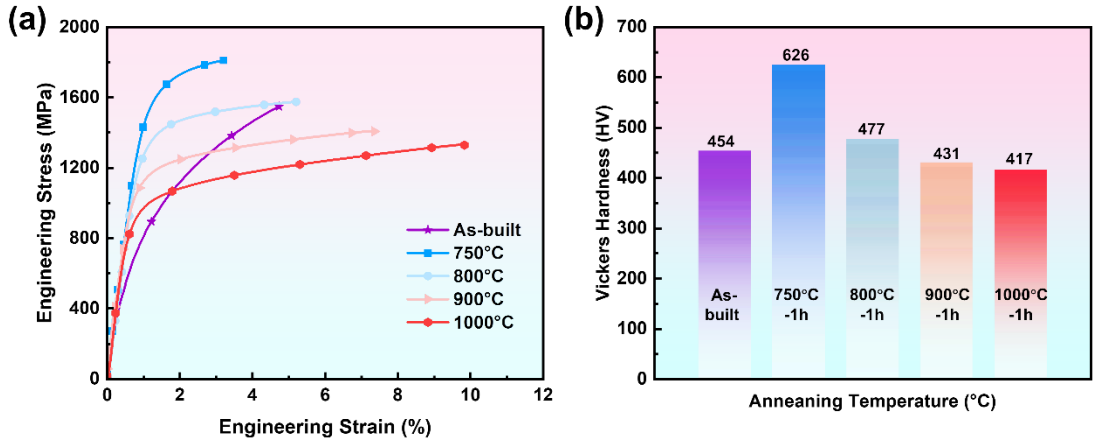


Figure 7 (a) The engineering stress-stain curves at room temperature of the as-built and annealed samples; (b) The Vickers hardness values at room temperature of the as-built and annealed samples.

Table 2 Tensile properties of the as-built and heat-treated samples

Alloy	Yield strength (MPa)	Ultimate tensile strength (MPs)	Elongation (%)
As-built	-	1549(±12)	4.7(±1.1)
750°C-1h	1355(±10)	1811(±18)	3.2(±0.6)
800°C-1h	1246(±6)	1575(±16)	5.2(±1.5)
900°C-1h	1035(±6)	1408(±10)	7.35(±1.9)
1000°C-1h	976(±9)	1332(±14)	9.8(±2.1)

The fractured surfaces after tensile testing were characterized by using SEM, as shown in Figure 8. It can be observed that all the fractured surfaces of as-built and heat-treated samples exhibit fine trench-like morphologies with fine dimples, which is the typical fractographic feature in HEAs with dual-phase eutectic structure [51]. During tensile deformation, the highly ductile FCC/$L1_2$ phase becomes thin, forming an upward edge. Conversely, the B2 phase is more brittle, resulting in the formation of the trench bottom [18, 28]. Notably, the fine dimples in the fractographs indicate the typical ductile fracture, which are formed by plastic deformation and local necking. Therefore, a mixed ductile and brittle fracture pattern occurs with the coexistence of dimples and trench-like morphology.

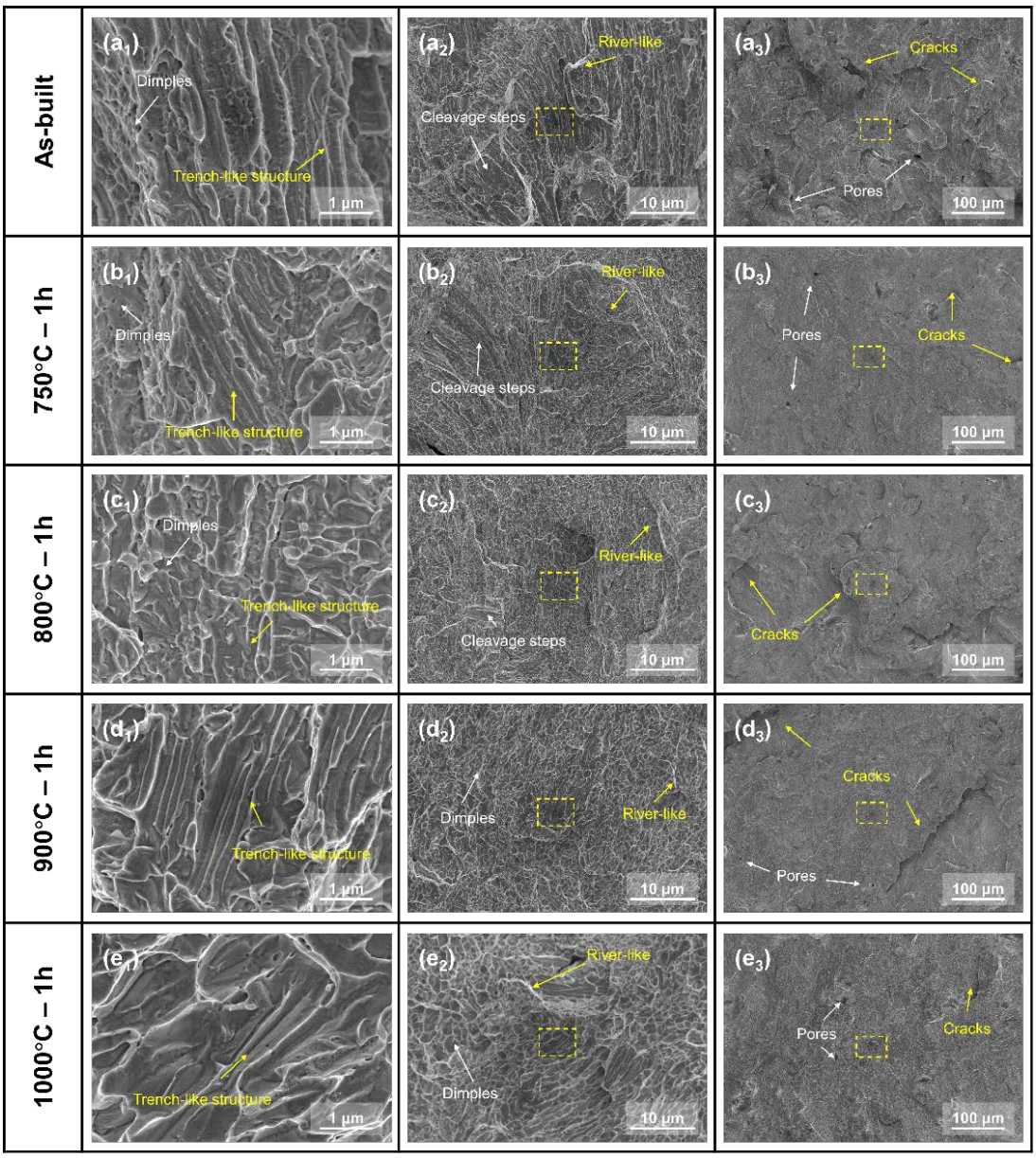


Figure 8 The fracture surface morphology of as-built and heat-treated samples

4 Discussion

4.1 Microstructure evolution

Figure 9 illustrates the microstructures of as-built $Ni_{30}Co_{30}Cr_{10}Fe_{10}Al_{18}W_2$ EHEA sample from different observing orientations. It is known that the growth direction of eutectic structure within the melt pool aligns with the direction of maximum heat flux during the printing process[28]. During the LPBF process, grains grow perpendicular to the melt pool boundary, which follows the thermal gradient direction and hence exhibits a typical columnar epitaxial growth. Specifically, a cell-like microstructure constituted by B2 blocks and thin FCC networks can be observed along the melt pool boundary in

the top surface of the as-built sample (Figures 9b and c). Correspondingly, a typical lamellar structure with eutectic colonies exhibiting various crystallographic orientations appears on the side of the as-built sample (Figures 9d and e).

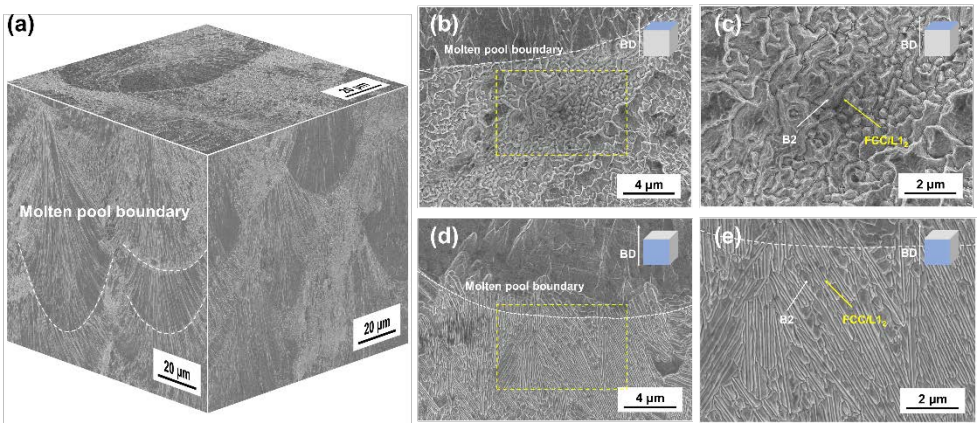


Figure 9 (a) The pseudo-3D microstructure of the as-built sample by SEM. SEM images of the microstructures close to the melt pool boundaries on the (b) top and (d) side surfaces of the as-built samples. (c) and (d) are the magnified SEM images of local microstructures selected in (b) and (d), respectively.

It is known that the high cooling rates of LPBF can bring about non-equilibrium solidification, leading to solute trapping within both FCC/$L1_2$ and B2 phases. During the solidification process, one phase of the eutectic alloy initially forms from the liquid, with its interface acting as nucleation site for the other phase. This process leads to the formation of lamellar structure through symbiotic growth of two phases [50]. It has also been observed that the B2 phase can act as the nucleation site for FCC phase (Figure 10), since the mixing enthalpy between Al and Ni is the most negative one (amongst all the constituent element binary combinations), facilitating the formation of AlNi phase [52, 53]. The FCC phase, on the contrary, is enriched in Co, Cr, Fe, and W, all of which share similar atomic radii and strong chemical compatibilities with each other [54].

In the B2 phase of the as-built sample, a modulated structure resulting from the spinodal decomposition has been identified, which is consistent with observations in several alloys within the Al–Co–Cr–Fe–Ni alloy system [55, 56]. Ren et al. [57] are the first to confirm the presence of compositional modulation within the B2 lamellae of the $AlCoCrFeNi_{2.1}$ alloy produced via LPBF. They proposed that the rapid and extreme solidification conditions characteristic of the LPBF process led to diffusion-limited solidification, resulting in supersaturated solid solutions. This, in turn, promotes spinodal decomposition within the B2 phase. Guo et al. [40] further suggested that the modulated structure significantly contributes to the strengthening of the $AlCoCrFeNi_{2.1}$

alloy, primarily through a mechanism known as spinodal hardening. This hardening arises from periodic fluctuations in lattice strain and shear modulus, induced by spinodal decomposition. These fluctuations create increased resistance to dislocation motion, thereby enhancing the overall strength of the alloy.

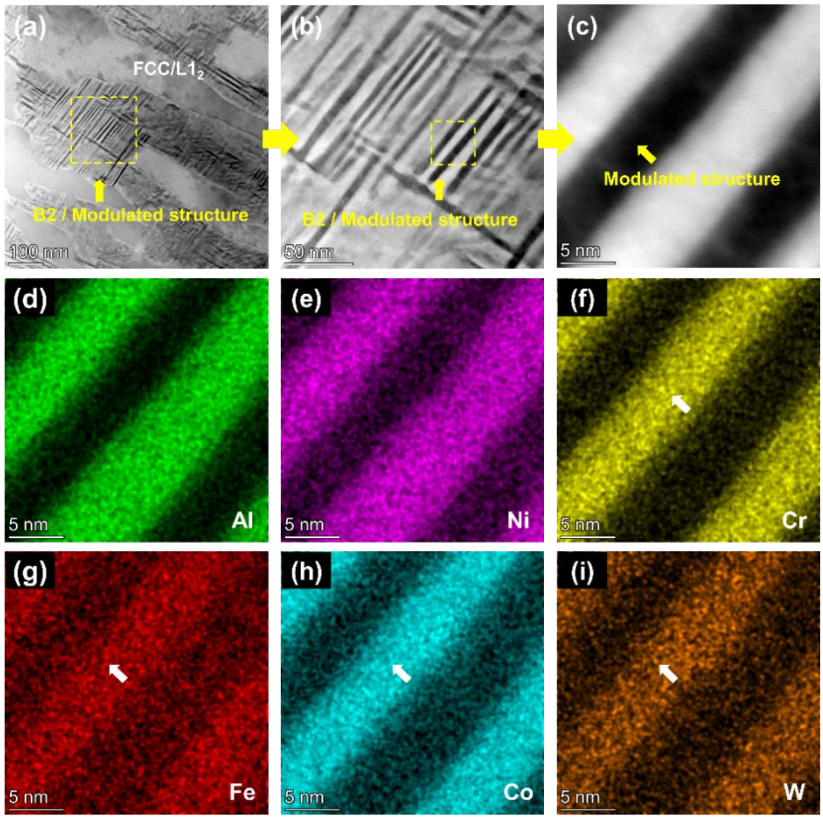


Figure 10 STEM analyses of the B2 phase. (a-c) HAADF STEM image of as-built sample. (d-i) EDX elemental mapping of Al, Ni, Co, Cr, Fe, W, respectively.

4.2 Microstructures of the heat-treated EHEAs

As evidenced in Figure 6, the microstructure of as-built sample changes significantly after heat treatment at 750 °C for 1 h, where the majority of dislocations arising from the LPBF process were eliminated (Figure 11). The SAED patterns display superlattice spots in both the FCC and BCC phases, indicating that the FCC phase contains ordered $L1_2$ precipitates, while the BCC phase is in an ordered B2 phase, same as as-built sample (Figure 11a). An increase in the average interlayer spacing of the FCC/$L1_2$ lamellae from 89 ±17 nm to 124 ±23 nm can be observed in the annealed sample, while the spacing of B2 lamellae decreases from 174 ±28 nm to 86 ±15 nm, as compared to those in the as-built sample (Figure 11b). Furthermore, the EDS mapping shows distinct elemental segregations between FCC/$L1_2$ and B2 phases, which is attributed to the interface migration at elevated temperatures (Figures 11c and d). Notably, the W-rich precipitates appear in the B2 phase, which could provide additional

strengthening effect [50]. As shown in Figure 11e, the average volume fraction of the nanoscale ordered $L1_2$ precipitates is around 10 ±1.76% due to elemental segregation within FCC/$L1_2$ phases. HRTEM image reveals that these nanoscale $L1_2$ precipitates exhibit a fully coherent crystallographic relationship with FCC phase. Strikingly, there is no elemental segregation within the B2 phase, which is the same as as-built sample (Figure 11f).

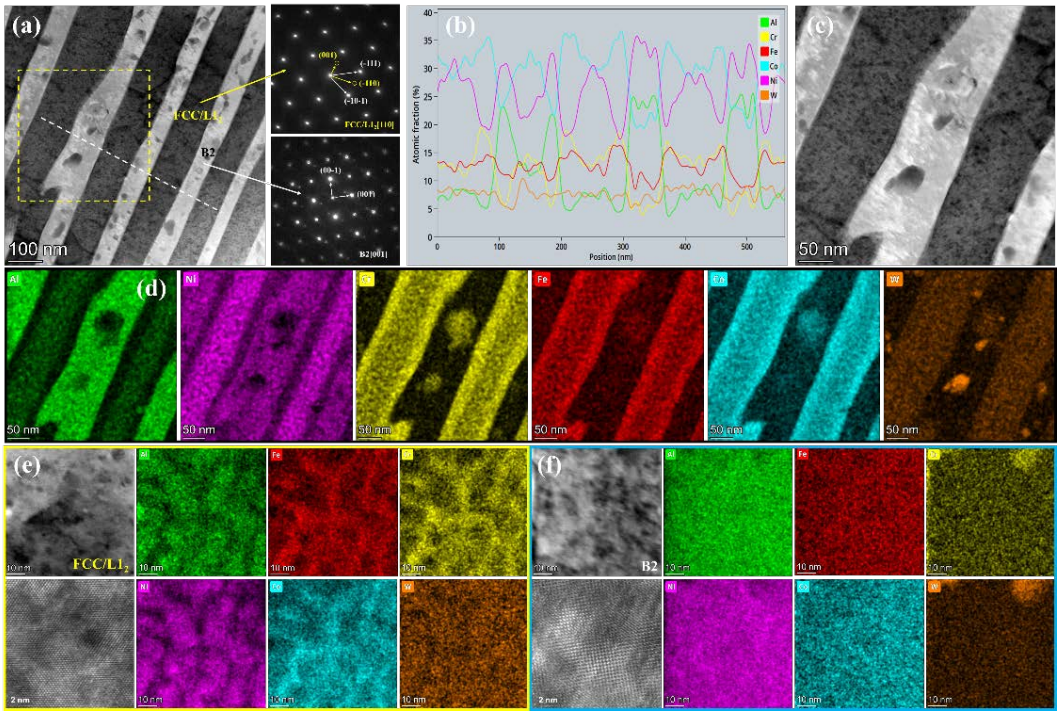


Figure 11 TEM analysis of the $Ni_{30}Co_{30}Cr_{10}Fe_{10}Al_{18}W_2$ EHEA sample after heat treatment at 750 °C for 1 h. (a) TEM image of heat treated EHEA sample with corresponding SAED patterns. (b) EDX line scanning along selected position in (a). (c, d) TEM and EDX elemetal mapping of selected heat treated EHEA sample. (e) STEM and HRTEM of FCC/$L1_2$ phase with corresponding EDX elemental mapping. (f) STEM and HRTEM of B2 phase with corresponding EDX elemental mapping.

In a sharp contrast, heat treatment at a higher temperature of 1000 °C for 1 h results in the complete disappearance of the ordered $L1_2$ precipitates, as evidenced by the absence of any additional superlattice spots in the SAED pattern in Figure 12a. The average interlayer spacings of both the FCC and B2 phases increase to 210 ±25 and 187 ±19 nm, respectively (Figure 12b). All the W-rich precipitates are eliminated as well, leading to an uniform elemental distribution in the disordered FCC and B2 phases, despite the pronounced elemental segregation between these dual-phase lamellae (Figure 12c-d).

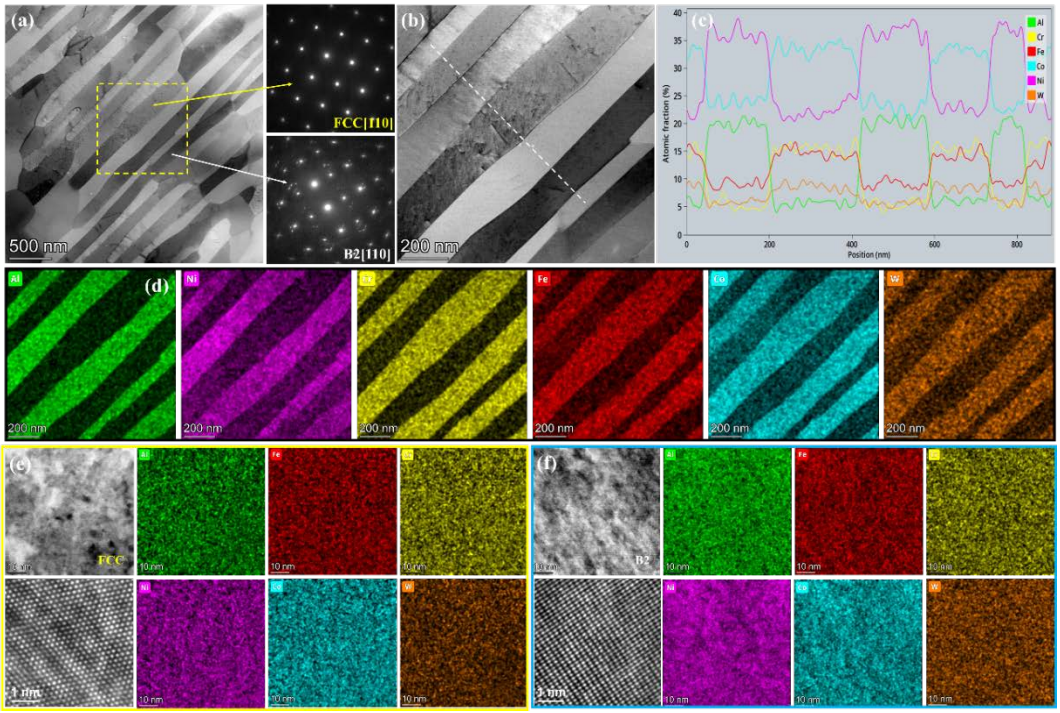


Figure 12 TEM analysis of the $Ni_{30}Co_{30}Cr_{10}Fe_{10}Al_{18}W_2$ EHEA sample after heat treatment at 1000 °C for 1 h. (a) TEM image of heat treated EHEA sample with corresponding SAED patterns. (b) Enlarged TEM image in selected region in (a). (c) EDX line scanning along selected position in (b). (d) EDX elemetal mapping of (b). (e) STEM and HRTEM of FCC phase with corresponding EDX elemental mapping. (f) STEM and HRTEM of B2 phase with corresponding EDX elemental mapping.

The overall microstructural features of the as-built and heat-treated samples are schematically illustrated in Figure 13. Initially, the interlayer spacings of FCC/$L1_2$ phase and B2 phase are 89 ±17 and 174 ±28 nm, respectively. These interlayers with very fine spacing, which is due to the rapid cooling rates inherent to LPBF [26], contribute significantly to the high strength of the as-built material by introducing numerous phase boundaries that impede dislocation motion [30]. However, the shortened mean free paths for dislocation glide can also restrict plastic deformation, adversely affecting ductility. Following the heat treatment at 750 °C for 1 h, the interlayer spacing of FCC/$L1_2$ phase increases to 124±23 nm, and that of B2 phase decreases to 86±15 nm, accompanied by the presence of W-rich nanoparticles within B2 phase. The increase in FCC/$L1_2$ interlayer spacing may reduce the number of phase boundaries, possibly decreasing the strength due to fewer obstacles for dislocation motion. Moreover, the $L1_2$ nanoparticles grow larger and the formation of W-rich nanoparticles introduces precipitation hardening, both of which increase the yield strength [50]. Furthermore, after heat treatment at 1000 °C for 1 h, microstructures become coarser

without the formation of precipitates. The interlayer spacing becomes 210 ±25 nm for the FCC phase and 187 ±19 nm for the B2 phase. The coarsening of the interlayer spacing leads to a reduction in the phase boundary area and the disappearance of the strengthening precipitates, allowing dislocations to move more freely and hence, results in a reduced strength. However, the reduced obstruction to dislocation movement could enhance ductility due to increased capacity for plastic deformation [57]. The significant changes in phase distribution, interlayer spacing, and elemental segregation of as-built EHEA are then annealing temperature determined.

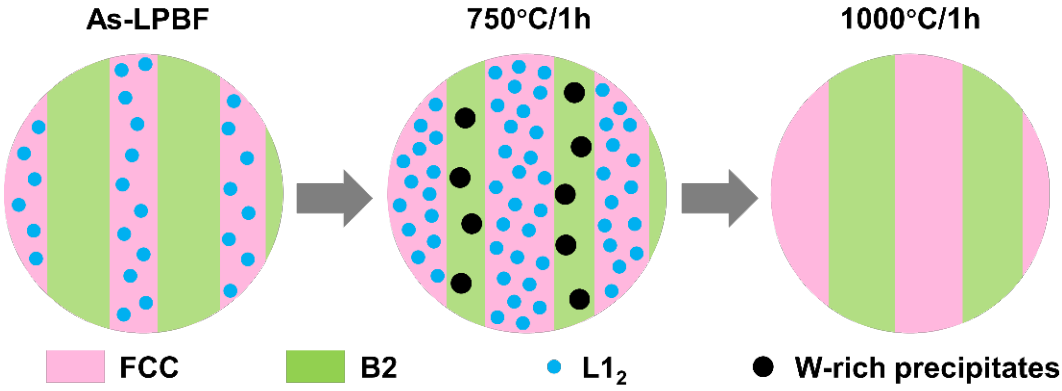


Figure 13 Schematic illustration of microstruture evolution mechanisms for as-built samples and heat treated samples.

4.3 Strengthening mechanisms

As demonstrated in Figure 7, the LPBF $Ni_{30}Co_{30}Cr_{10}Fe_{10}Al_{18}W_2$ EHEA exhibits high strength and ductility, which can be attributed to two primary strengthening mechanisms. Firstly, the ultrafine eutectic structure in the as-built EHEA because of the rapid solidification. Such refined microstructure results in a superior mechanical performance, serving as the primary crucial strengthening mechanism. Secondly, the dislocation mobility is resisted by the highly coherent FCC/B2 phase boundaries, resulting in enhanced strength. During tensile deformation, the back stress is generated by the phase boundaries can also improve the tensile strength. Additionally, there are extensive dislocation slips, stacking faults (SFs), and Lomer-Cottrell (L-C) locks during deformation within FCC phase. These combined mechanisms of grain refinement and dislocation movement hindering contribute to the exceptional mechanical performance of the as-built $Ni_{30}Co_{30}Cr_{10}Fe_{10}Al_{18}W_2$ EHEA.

It is known that grain refinement is a widely used method to increase the strength of materials. By reducing the average grain size, the number of grain boundaries in the material increases. These grain boundaries act as strong pinning points to dislocation movement, which is a primary mechanism of deformation in metals. This relationship

between grain size and strength is described by the Hall-Petch equation[58]:

$$\Delta\sigma_G = k_y \lambda^{-1/2} \tag{2}$$

Where k_y is the Hall-Petch coefficient, for which the value of 371 MPa μm$^{1/2}$ from the $Al_{0.1}$CoCrFeNi system is used [59].

The contribution from dislocation strengthening in the FCC/$L1_2$ and B2 phases can be expressed using Bailey-Hirsch equation [60]:

$$\Delta\sigma_D = M\alpha Gb\rho^{1/2} \tag{3}$$

where $\Delta\sigma_D$ is the strengthening contribution from dislocations. M represents the orientation Taylor factor with 3.06 for FCC phase and 2.87 for B2 phase [61, 62]. α is a constant, which is 0.2 for FCC phase and 0.24 for B2 phase [63, 64]. G is the shear modulus, which is 76.9 GPa for FCC phase and 80 GPa for B2 phase [62, 65]. b is the magnitude of Burgers vector for a full dislocation, which is 0.255 nm for FCC phase and 0.248 nm for B2 phase [50, 66]. ρ is the dislocation density, which can be approximated as the density of geometrically necessary dislocations (GNDs), ρ_{GND}. Based on the EBSD measurement, ρ_{GND} can be calculated as [67]:

$$\rho_{GND} = \frac{2\theta}{\mu b} \tag{4}$$

where θ is the local mis-orientation angle from the EBSD data, and μ is the step size (40 nm).

The overall dislocation strengthening can be estimated by [63]:

$$\sigma_D = f_{FCC}\sigma_{FCC} + f_{B2}\sigma_{B2} \tag{5}$$

where σ_D represents the total strength due to dislocation strengthening. f_{FCC} and f_{B2} are the volume fractions of FCC and B2 phases, respectively. σ_{FCC} and σ_{B2} are the contribution strength of the dislocation strengthening in the FCC and B2 phases, respectively.

In addition to those strengthening mechanisms mentioned, the nano-precipitates within both FCC and B2 phases also contribute significantly to the mechanical properties strengthening, especially in heat-treated samples. The overall increase in strength due to precipitation strengthening can be estimated as [63]:

$$\sigma_p = \nu_{FCC}\Delta\sigma_{FCC} + \nu_{B2}\Delta\sigma_{B2} \tag{6}$$

where v_{FCC} and v_{B2} are the volume fraction of FCC and B2 phases, respectively. $\Delta\sigma_{FCC}$ is the contribution of $L1_2$ precipitates to the strength of FCC phase, and $\Delta\sigma_{B2}$ is the contribution of W precipitates to the strength of B2 phase.

The precipitates in the matrix enhance the strength of alloy by impeding the movement of dislocations, and this is known as precipitation strengthening. Based on the interaction between the precipitates and dislocations, precipitation strengthening can be divided into two main categories: the Orowan bypass mechanism ($\Delta\sigma_{orw}$) and shearing mechanisms ($\Delta\sigma_{shearing}$) [68]. However, these two mechanisms cannot coexist. The type of precipitation strengthening is determined by the resistance of dislocation slip. Ultimately, the mechanism with smaller resistance is the precipitation strengthening effect:

$$\Delta\sigma_p = min(\Delta\sigma_{orw}, \Delta\sigma_{shearing}) \tag{7}$$

The Orowan bypass mechanism typically occurs in precipitates that are larger in size or incoherent with the matrix, which can be described as [63]:

$$\Delta\sigma_{orw} = M\frac{0.4Gb}{\pi\sqrt{1-v}}\frac{ln(2r_m/b)}{\lambda_p} \tag{8}$$

where v is the Poisson's ratio, taken as 0.25. The modified radius r_m is given by $r_m=(2/3)^{0.5}r$, where r is the average radius of precipitates. The spacing of precipitates (λ_p) is given by $\lambda_p = 2r_m(\sqrt{\pi/4f} - 1)$, where f is the volume fraction of precipitates.

The shearing mechanism, on the contrary, typically occurs in precipitates that are relatively small in size or coherent with the matrix. Coherency strengthening ($\Delta\sigma_{CS}$), modulus strengthening ($\Delta\sigma_{MS}$) and ordering strengthening ($\Delta\sigma_{OS}$) are three types of strengthening mechanisms as:

$$\Delta\sigma_{cs} = M\alpha_\varepsilon(G\varepsilon_c)^{3/2}(\frac{rf}{0.5Gb})^{1/2} \tag{9}$$

$$\Delta\sigma_{MS} = 0.0055M(\Delta G)^{3/2}(\frac{2f}{G})^{1/2}(\frac{r}{b})^{\frac{3m}{2}-1} \tag{10}$$

$$\Delta\sigma_{os} = 0.81M\frac{\gamma_{APB}}{2b}(\frac{3\pi f}{8})^{1/2} \tag{11}$$

where ε_c is the constrained lattice parameter mismatch, expressed as $\varepsilon_c=2/3\varepsilon$ with ε taken as 0.084% for the $L1_2$ precipitate in FCC matrix [69]. G is the shear modulus with 76.9 GPa for FCC [65]. $\Delta G = |G-G_p|$ represents the shear modulus mismatch between the precipitate and matrix, where G_p is 90.2 GPa for the $L1_2$ precipitates [70]. The constant m is 0.85 [71]. The anti-phase boundary energy γ_{APB} for the $L1_2$ precipitate is 175 mJ/m^2 [70]. The mean particle size r is 1 nm and 1.9 nm for the $L1_2$ precipitates in as-built and heat-treated samples at 750 °C for 1 h, respectively. The relative volume fraction of precipitates within the matrix (f) is 10% and 15% for $L1_2$ precipitates of as-built and heat-treated samples, respectively.

The calculated results of $\Delta\sigma_{orw}$, $\Delta\sigma_{CS}$, $\Delta\sigma_{MS}$, and $\Delta\sigma_{OS}$ for precipitation strengthening are summarized in Table 3. The strengthening of $L1_2$ nanoparticles calculated via the shearing mechanism is less than that of the Orowan bypass mechanism, indicating that the shearing mechanism should be the effective mechanism for $L1_2$ precipitate. Notably, the Orowan bypass mechanism is an effective mechanism for W-rich precipitate. Therefore, the final strengthening of $L1_2$ precipitates in the FCC matrix is in 142.8 MPa, while the strengthening of W-rich precipitates in the B2 matrix is in 102.8 MPa.

Above all, the yield strength of both as-built and heat-treated $Ni_{30}Co_{30}Cr_{10}Fe_{10}Al_{18}W_2$ is predominantly governed by the refined nano-lamellar structure. The yield strength is further enhanced by the pre-existing dislocations, the ordered $L1_2$ structures, and W-rich precipitates. Consequently, the overall yield strength of EHEA can be represented as follows:

$$\sigma_y = \sigma_0 + \Delta\sigma_G + \Delta\sigma_D + \Delta\sigma_p \tag{11}$$

where σ_0 is the intrinsic lattice friction stress, which takes the value of 95 MPa from $Al_{0.3}CoCrFeNi$ [72]. The results indicate that fine grain strengthening is the predominant mechanism for the overall strengths in both the as-built and heat treat samples.

The results of overall strengthening are summarized in Table 3. The 750 °C annealed sample shows better strength than as-built because of more precipitation strengthening.

Table 3 Contribution of different strengthening mechanisms to yield strength of as-built and heat-treated samples

	$\Delta\sigma_G$ (MPa)	$\Delta\sigma_D$ (MPa)	Phase	$\Delta\sigma_{orw}$ (MPa)	$\Delta\sigma_{CS}$ (MPa)	$\Delta\sigma_{MS}$ (MPa)	$\Delta\sigma_{OS}$ (MPa)	σ_y (MPa)
As-built	723.4	395.5	FCC B2		7.2	60.6	291.8	1142.6
750	809.6	352.9	FCC B2	142.8	10.9	91.9	442.6	1291.3
1000	588.8	264.6	FCC B2					853.4

In summary, the high yield strength of the $Ni_{30}Co_{30}Cr_{10}Fe_{10}Al_{18}W_2$ EHEA produced using LPBF is primarily attributable to the fine nanolamellar structure that forms due to the rapid solidification process inherent to L-PBF (723.4 MPa) and is

further strengthened by the existing dislocations (395.5 MPa) and ordered $L1_2$ phases (23.7 MPa). After the heat treatment at 750 °C, the contributions from grain refinement and dislocation strengthening are 809.6 and 352.9 MPa, respectively. The precipitation strengthening of the $L1_2$ and W-rich precipitates is 128.8 MPa, which enhance the yield strength to 1291.3 MPa. However, when heat treated at 1000 °C, both the coarsening of interlayer spacing and the dissolution of precipitates occur, leading to a lower yield strength of 853.4 MPa.

4.4 Deformation mechanisms

To elucidate the deformation behavior of both the as-built and heat-treated sample, the scanning TEM (STEM) and HRTEM were conducted, as illustrated in Figure 14. In comparison with the as-built sample, the activation of stacking faults (SFs) and Lomer-Cottrell (L-C) locks is more pronounced in the heat-treated sample at 1000 °C. Previous studies on $Ni_{40}Co_{20}Fe_{10}Cr_{10}Al_{18}W_2$ [50] indicated that Al and Ni are the elements associated with high stacking-fault energy (SFE). During the heat treatment process, atomic diffusion and element partitioning occur, resulting in decreased Al and Ni contents in the FCC phase. Consequently, the heat-treated FCC phase exhibits a lower SFE compared to that in the as-built sample. The K-S orientation relationship between the FCC and B2 phases creates a semi-coherent interface, indicating that the deformation behavior of the FCC phase is significantly influenced by the B2 phase [73, 74]. This interaction leads to increased stress concentration at the FCC/B2 interfaces, which promotes stress-induced martensitic transformation (SIMT) in the B2 phase, enhancing its work-hardening ability and strength [59]. Additionally, the formation of SFs at the interface induces further stress[75], accelerating dislocation nucleation and multiplication in the B2 phase, thereby contributing to its work-hardening capacity. Furthermore, heat treatment may impact the stability of the B2 phase by altering its interface with the FCC phase [30, 76]. Improved interface stability can reduce stress concentration, enhance overall mechanical performance, and prevent premature failure of the B2 phase.

Moreover, during heat treatment, lamellar structure becomes significantly coarsened and all precipitates are dissolved, leading to a further reduction in effective stress and back stress. As a result, the elongation of material increases with increasing heat-treatment temperature.

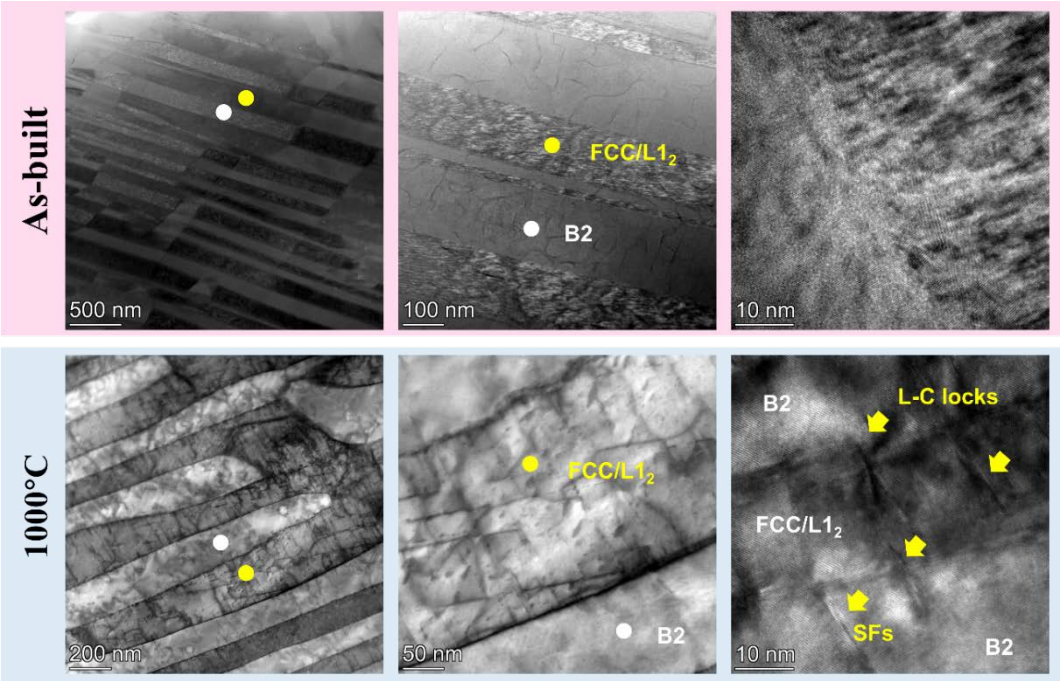


Figure 14 TEM images of deformed microstructures in as-built sample and heat-treated sample.

5. Summary

$Ni_{30}Co_{30}Cr_{10}Fe_{10}Al_{18}W_2$ EHEA was successfully fabricated using LPBF, demonstrating a high UTS. Effects of heat treatment on microstructures and mechanical properties are systematically studied, where the main conclusions are:

(1) The microstructures of as-built sample exhibit a typical epitaxial growth from the fusion line with featured columnar grains. Two phases of FCC/$L1_2$ and B2 can be observed. The volume fractions of FCC/$L1_2$ and B2 phases are 31.9% and 68.1%, respectively. The interlayer spacing is approximately 89±17 nm for FCC and 174±28 nm for B2.

(2) Heat treatment at 750 °C for 1 h results in the transformation of B2 matrix into FCC matrix. The volume fractions of FCC/$L1_2$ and B2 phases are 82.2% and 17.8%, respectively. Within the B2 phase, tungsten-rich precipitates are observed. As the temperature increases, the microstructures coarsen, accompanied with increased lamellar spacing in the eutectic structure. After heat treatment at 1000 °C for 1 h, depletion of super lattice $L1_2$ and tungsten-rich precipitates occur.

(3) As-built sample shows no distinct yield strength and UTS of 1548 MPa with elongation of 5.2%. After heat treatment at 750 °C for 1 h, the UTS increases to 1811 MPa, whereas the elongation decreases to 2%. After heat treatment at temperatures above 800 °C for 1 h, both UTS and elongation are improved. When temperature is

elevated to 1000 °C, the UTS decreases, but the elongation increases significantly to 9.32%.

(4) The tensile fractography of as-built and heat-treated samples indicates a mixed fracture mode, which exhibits a fine trench-like morphology with some fine dimples, showing both ductile and brittle behaviors.

These investigations provide insights for advancing the additive manufacturing of high-performance EHEAs. Microstructural tuning through heat treatment can result in the successful optimization of mechanical properties of EHEAs, which can pave the way for their potential applications in aerospace and automotive engineering.

Acknowledgements

This work was financially supported by National Natural Science Foundation of China (Grant No. 52405395), National Key Research and Development Program of China (No. 2022YFB4602102), Agency for Science, Technology and Research (A*STAR) of Singapore via Structural Metal Alloys Programme (No. A18B1b0061) and Advanced Models for Additive Manufacturing (No. M22L2b0111). The authors would like to thank Zhe Xie from the Instrumental Analysis Center of Shanghai Jiao Tong University for the assistance EBSD characterization and Yuchao Wu from KAIPLE Co. Ltd for the assistance with TEM characterization.

References

[1] Y. Zhang, T.T. Zuo, Z. Tang, M.C. Gao, K.A. Dahmen, P.K. Liaw and Z.P. Lu, Microstructures and Properties of High-Entropy Alloys, Prog. Mater. Sci. 61 (2014) 1-93. https://doi.org/10.1016/j.pmatsci.2013.10.001.

[2] J.W. Yeh, S.K. Chen, S.J. Lin, J.Y. Gan, T.S. Chin, T.T. Shun, C.H. Tsau and S.Y. Chang, Nanostructured High Entropy Alloys with Multiple Principal Elements: Novel Alloy Design Concepts and Outcomes, Adv. Eng. Mater. 6 (2004) 299-303. https://doi.org/https://doi.org/10.1002/adem.200300567.

[3] B. Cantor, I.T.H. Chang, P. Knight and A.J.B. Vincent, Microstructural Development in Equiatomic Multicomponent Alloys, Mater. Sci. Eng.: A. 375 (2004) 213-218. https://doi.org/10.1016/j.msea.2003.10.257.

[4] B. Gludovatz, A. Hohenwarter, D. Catoor, E.H. Chang, E.P. George and R.O. Ritchie, A Fracture-Resistant High-Entropy Alloy for Cryogenic Applications, Science. 345 (2014) 1153-1158. https://doi.org/doi:10.1126/science.1254581.

[5] P. Kumar, S. Huang, D.H. Cook, K. Chen, U. Ramamurty, X.P. Tan and R.O. Ritchie, A Strong Fracture-Resistant High-Entropy Alloy with Nano-Bridged Honeycomb Microstructure Intrinsically Toughened by 3D-Printing, Nat. Commun. 15 (2024) 841. https://doi.org/10.1038/s41467-024-45178-2.

[6] P. Kumar, M. Michalek, D.H. Cook, H. Sheng, K.B. Lau, P. Wang, M. Zhang, A.M. Minor, U. Ramamurty and R.O. Ritchie, On the Strength and Fracture Toughness of an Additive Manufactured CrCoNi Medium-Entropy Alloy, Acta Mater. 258 (2023) 119249. https://doi.org/https://doi.org/10.1016/j.actamat.2023.119249.

[7] S.D. Lu, X.X. Li, X.Y. Liang, J.H. He, W.T. Shao, K.H. Li and J. Chen, Effect of Y Additions on the Oxidation Behavior of Vacuum Arc Melted Refractory High-Entropy Alloy $AlMo_{0.5}NbTa_{0.5}TiZr$ at Elevated Temperatures, Vacuum. 201 (2022) 111069. https://doi.org/10.1016/j.vacuum.2022.111069.

[8] X.Y. Fu, C.Z. Wan, H.Z. Huyan, S.B. Wang, A. Zhang, J.X. Zhou, H.T. Zhang, X. Zhao, J. Chen, X.Q. Pan, Y. Huang and X.F. Duan, Medium Entropy Alloy Wavy Nanowires as Highly Effective and Selective Alcohol Oxidation Reaction Catalysts for Energy-Saving Hydrogen Production and Alcohol Upgrade, EES Catalysis. (2024) https://doi.org/10.1039/d4ey00090k.

[9] S. Thapliyal, S.S. Nene, P. Agrawal, T.H. Wang, C. Morphew, R.S. Mishra, B.A. McWilliams and K.C. Cho, Damage-Tolerant, Corrosion-Resistant High Entropy Alloy with High Strength and Ductility by Laser Powder Bed Fusion Additive Manufacturing, Addit. Manuf. 36 (2020) 101455. https://doi.org/10.1016/j.addma.2020.101455.

[10] Y. Zhao, D.H. Lee, M.Y. Seok, J.A. Lee, M.P. Phaniraj, J.Y. Suh, H.Y. Ha, J.Y. Kim, U. Ramamurty and J.i. Jang, Resistance of CoCrFeMnNi High-Entropy Alloy to Gaseous Hydrogen Embrittlement, Scr. Mater. 135 (2017) 54-58. https://doi.org/https://doi.org/10.1016/j.scriptamat.2017.03.029.

[11] Y. Zhao, J.M. Park, D.H. Lee, E.J. Song, J.Y. Suh, U. Ramamurty and J.i. Jang, Influences of Hydrogen Charging Method on the Hydrogen Distribution and Nanomechanical Properties of Face-centered Cubic High-Entropy Alloy: A Comparative Study, Scr. Mater. 168 (2019) 76-80. https://doi.org/https://doi.org/10.1016/j.scriptamat.2019.04.025.

[12] S.H. Li, D.H. Lee, Y.K. Zhao and U. Ramamurty, Hydrogen-induced Softening and Embrittlement in 316L Stainless Steel Fabricated Using Laser-Powder Bed Fusion, Acta Mater. 274 (2024) 145795. https://doi.org/10.1016/j.actamat.2024.119959.

[13] G. Velisa, F. Granberg, E. Levo, Y. Zhou, Z. Fan, H. Bei, F. Tuomisto, K. Nordlund, F. Djurabekova, W.J. Weber and Y. Zhang, Recent Progress on Understanding the Temperature-Dependent Irradiation Resistance Ranking Among NiFe, NiCoCr, and NiCoFeCr alloys: A review, J. Mater. Res. 38 (2023) 1510-1526. https://doi.org/10.1557/s43578-023-00922-0.

[14] Z. Zhang, Z.X. Su, B.Z. Zhang, Q. Yu, J. Ding, T. Shi, C.Y. Lu, R.O. Ritchie and E. Ma, Effect of Local Chemical Order on the Irradiation-Induced Defect Evolution in CrCoNi Medium-Entropy Alloy, Proc. Natl. Acad. Sci. U. S. A. 120 (2023) 2218673120. https://doi.org/10.1073/pnas.2218673120.

[15] S.Y. Wei, Y.K. Zhao, B.C. Zhang, P. Wang and U. Ramamurty, Mesoscopic Chemical Heterogeneities in Laser Powder Bed Fused CoCrMo and Ni Mixed Powders and Their Effect on the Mechanical Properties, Mater. Sci. Eng.: A. 888 (2023) 145795. https://doi.org/https://doi.org/10.1016/j.msea.2023.145795.

[16] R. Duan, J.T. Xu, Y.K. Zhao, Q.J. Zhou, Z.Y. Yan, Y. Xie, P. Dong, L.F. Xu, K. Feng, Z.G. Li, X.B. Liang and U. Ramamurty, High Entropy Alloys Amenable for Laser Powder Bed Fusion: A Thermodynamics Guided Machine Learning Search, Addit. Manuf. 86 (2024) 104195. https://doi.org/10.1016/j.addma.2024.104195.

[17] Y.P. Lu, Y. Dong, S. Guo, L. Jiang, H.J. Kang, T.M. Wang, B. Wen, Z.J. Wang, J.C. Jie, Z.Q. Cao, H.H. Ruan and T.J. Li, A Promising New Class of High Temperature Alloys: Eutectic High Entropy Alloys, Sci. Rep. 4 (2014) 1-5. https://doi.org/10.1038/srep06200.

[18] Y.P. Lu, X.Z. Gao, L. Jiang, Z.N. Chen, T.M. Wang, J.C. Jie, H.J. Kang, Y.B. Zhang, S. Guo, H.H. Ruan, Y.H. Zhao, Z.Q. Cao and T.J. Li, Directly Cast Bulk Eutectic and Near-Eutectic High Entropy Alloys with Balanced Strength and Ductility in a Wide Temperature Range, Acta Mater. 124 (2017) 143-150. https://doi.org/10.1016/j.actamat.2016.11.016.

[19] T. Özel, H. Shokri and R. Loizeau, A Review on Wire-Fed Directed Energy Deposition Based Metal Additive Manufacturing, J. Manuf. Mater. Proc. 7 (2023) 45. https://doi.org/10.3390/jmmp7010045.

[20] S.H. Li, P. Kumar, S. Chandra and U. Ramamurty, Directed Energy Deposition of Metals: Processing, Microstructures, and Mechanical Properties, Int. Mater. Rev. (2022) 1-43. https://doi.org/doi:10.1080/09506608.2022.2097411.

[21] S.Y. Wu, D.X. Qiao, H.L. Zhao, J. Wang and Y.P. Lu, A Novel $NbTaW_{0.5}(Mo_2C)_x$ Refractory High Entropy Alloy with Excellent Mechanical Properties, J. Alloys Compd. 889 (2021) 161800. https://doi.org/https://doi.org/10.1016/j.jallcom.2021.161800.

[22] M. Zhang, E.P. George and J.C. Gibeling, Elevated-Temperature Deformation Mechanisms in a CrMnFeCoNi High-Entropy Alloy, Acta Mater. 218 (2021) 117181. https://doi.org/10.1016/j.actamat.2021.117181.

[23] J.W. Miao, H.W. Yao, J. Wang, Y.P. Lu, T.M. Wang and T.J. Li, Surface Modification for $AlCoCrFeNi_{2.1}$ Eutectic High-Entropy Alloy via Laser Remelting Technology and Subsequent Aging Heat Treatment, J. Alloys Compd. 894 (2022) 162380. https://doi.org/10.1016/j.jallcom.2021.162380.

[24] J. Zhou, H.C. Liao, H. Chen and A.J. Huang, Carbon-Alloyed $Fe_{35}Mn_{10}Cr_{20}Ni_{35}$ High Entropy a Alloy Synthesized by Mechanical Alloying Plus Spark Plasma Sintering, J. Alloys Compd. 859 (2021) 157851. https://doi.org/https://doi.org/10.1016/j.jallcom.2020.157851.

[25] D. Karlsson, A. Marshal, F. Johansson, M. Schuisky, M. Sahlberg, J.M. Schneider and U. Jansson, Elemental Segregation in An AlCoCrFeNi High-Entropy Alloy-A Comparison Between Selective Laser Melting and Induction Melting, J. Alloys Compd. 784 (2019) 195-203. https://doi.org/10.1016/j.jallcom.2018.12.267.

[26] W.E. King, A.T. Anderson, R.M. Ferencz, N.E. Hodge, C. Kamath, S.A. Khairallah and A.M. Rubenchik, Laser Powder Bed Fusion Additive Manufacturing of Metals; Physics, Computational, and Materials Challenges, Appl. Phys. Rev. 2 (2015) 041304. https://doi.org/10.1063/1.4937809.

[27] S.A. Khairallah, A.T. Anderson, A. Rubenchik and W.E. King, Laser Powder Bed Fusion Additive Manufacturing: Physics of Complex Melt Flow and Formation Mechanisms of Pores, Spatter, and Denudation Zones, Acta Mater. 108 (2016) 36-45. https://doi.org/https://doi.org/10.1016/j.actamat.2016.02.014.

[28] L. He, S.W. Wu, A.P. Dong, H.B. Tang, D.F. Du, G.L. Zhu, B.D. Sun and W.T. Yan, Selective Laser Melting of Dense and Crack Free $AlCoCrFeNi_{2.1}$ Eutectic High Entropy Alloy: Synergizing Strength and Ductility, J. Mater. Sci. Technol. 117 (2022) 133-145. https://doi.org/10.1016/j.jmst.2021.11.049.

[29] L.W. Lan, W.X. Wang, Z.Q. Cui, X.H. Hao and D. Qiu, Anisotropy Study of the Microstructure and Properties of $AlCoCrFeNi_{2.1}$ Eutectic High Entropy Alloy Additively Manufactured by Selective Laser Melting, J. Mater. Sci. Technol. 129 (2022) 228-239. https://doi.org/10.1016/j.jmst.2022.04.020.

[30] Y.N. Guo, H.J. Su, H.T. Zhou, Z.L. Shen, Y. Liu, J. Zhang, L. Liu and H.Z. Fu, Unique Strength-Ductility Balance of $AlCoCrFeNi_{2.1}$ Eutectic High Entropy Alloy with Ultra-Fine Duplex Microstructure Prepared by Selective Laser Melting, J. Mater. Sci. Technol. 111 (2022) 298-306. https://doi.org/10.1016/j.jmst.2021.10.013.

[31] S.Y. Wei, C. Hutchinson and U. Ramamurty, Mesostructure Engineering in Additive Manufacturing of Alloys, Scr. Mater. 230 (2023) 115429. https://doi.org/https://doi.org/10.1016/j.scriptamat.2023.115429.

[32] L. Wang, M.X. Wu, H.Y. Chen, W. Hang, X. Wang, Y.X. Han, H. Chen, P.Q. Chen, T.H. Beri, L.M. Luo and B.H. Lyu, Damage Evolution and Plastic Deformation Mechanism of Passivation Layer During Shear Rheological Polishing of Polycrystalline Tungsten, J. Mater. Res. Technol. 28 (2024) 1584-1596. https://doi.org/https://doi.org/10.1016/j.jmrt.2023.12.122.

[33] H.Y. Chen, L. Wang, F. Peng, Q. Xu, Y.X. Xiong, S.J. Zhao, K. Tokunaga, Z.G. Wu, Y. Ma, P.Q. Chen, L.M. Luo and Y.C. Wu, Hydrogen Retention and Affecting Factors in Rolled Tungsten: Thermal Desorption Spectra and Molecular Dynamics Simulations, Int. J. Hydrogen Energ. 48 (2023) 30522-30531. https://doi.org/https://doi.org/10.1016/j.ijhydene.2023.03.151.

[34] R. Duan, Y.K. Zhao, J.T. Xu, Q.J. Zhou, Z.Y. Yan, Y. Xie, P. Dong, K. Feng, Z.G. Li, B.B. Xu, X.B. Liang and U. Ramamurty, Additive Manufacturing of Refractory Multi-Principal Element Alloy with Ultrahigh-Temperature Strength via Simultaneous Enhancements in Printability and Solid Solution Hardening, Addit. Manuf. 91 (2024) 104340. https://doi.org/10.1016/j.addma.2024.104340.

[35] Q.F. Wu, Z.J. Wang, X.B. Hu, T. Zheng, Z.S. Yang, F. He, J.J. Li and J.C. Wang, Uncovering the Eutectics Design by Machine Learning in the Al-Co-Cr-Fe-Ni High Entropy System, Acta Mater. 182 (2020) 278-286. https://doi.org/10.1016/j.actamat.2019.10.043.

[36] F. Yang, L.L. Wang, Z.J. Wang, Q.F. Wu, K.X. Zhou, X. Lin and W.D. Huang, Ultra Strong and Ductile Eutectic High Entropy Alloy Fabricated by Selective Laser Melting, J. Mater. Sci. Technol. 106 (2022) 128-132. https://doi.org/10.1016/j.jmst.2021.08.015.

[37] S. Chandra, J. Radhakrishnan, S. Huang, S. Wei and U. Ramamurty, Solidification in Metal Additive Manufacturing: Challenges, Solutions, and Opportunities, Prog. Mater. Sci. 148 (2025) 101361. https://doi.org/https://doi.org/10.1016/j.pmatsci.2024.101361.

[38] J.T. Xu, M. Qin, S.Z. Du, P. Kumar, J. Zhu, Y.B. Jia, Z.Y. Yan, Y. Xie, P. Dong, K. Feng, Z.G. Li, Q.J. Zhou, X.B. Liang and U. Ramamurty, Enhancing the Strength and Plasticity of Laser Powder Bed Fused NbMoTaW Refractory High-Entropy Alloy via Ti Alloying, J. Alloys Compd. 1001 (2024) 104340. https://doi.org/10.1016/j.jallcom.2024.175043.

[39] H. Khodashenas and H. Mirzadeh, Post-Processing of Additively Manufactured High-Entropy Alloys - A Review, J. Mater. Res. Technol. 21 (2022) 3795-3814. https://doi.org/https://doi.org/10.1016/j.jmrt.2022.11.027.

[40] Y.N. Guo, H.J. Su, H.L. Gao, Z.L. Shen, P.X. Yang, Y. Liu, D. Zhao, Z. Zhang and M. Guo, Insight into Annealing-Induced Hardening and Softening Behaviors in a Laser Powder-bed Fusion Printed In-situ Composite Eutectic High-entropy Alloy, Compos. Part B-Eng. 281 (2024) 111523. https://doi.org/https://doi.org/10.1016/j.compositesb.2024.111523.

[41] D. Vogiatzief, A. Evirgen, S. Gein, V.R. Molina, A. Weisheit and M. Pedersen, Laser Powder Bed Fusion and Heat Treatment of an $AlCrFe_2Ni_2$ High Entropy Alloy, Front. Mater. 7 (2020) 1-12. https://doi.org/10.3389/fmats.2020.00248.

[42] C.C. Zhang, K. Feng, H. Kokawa, B.L. Han and Z.G. Li, Cracking Mechanism and Mechanical Properties of Selective Laser Melted CoCrFeMnNi High Entropy Alloy Using Different Scanning Strategies, Mater. Sci. Eng.: A. 789 (2020) 139672. https://doi.org/10.1016/j.msea.2020.139672.

[43] D.D. Gu, Y.C. Hagedorn, W. Meiners, G.B. Meng, R.J.S. Batista, K. Wissenbach and R. Poprawe, Densification Behavior, Microstructure Evolution, and Wear Performance of Selective Laser Melting Processed Commercially Pure Titanium, Acta Mater. 60 (2012) 3849-3860.

https://doi.org/10.1016/j.actamat.2012.04.006.

[44] Q. Cheng, Y. Zhang, X.D. Xu, D. Wu, S. Guo, T.G. Nieh and J.H. Chen, Mechanistic Origin of Abnormal Annealing Induced Hardening in an $AlCoCrFeNi_{2.1}$ Eutectic Multi Principal Element Alloy, Acta Mater. 252 (2023) 118905. https://doi.org/10.1016/j.actamat.2023.118905.

[45] Q.F. Wu, F. He, J.J. Li, H.S. Kim, Z.J. Wang and J.C. Wang, Phase Selective Recrystallization Makes Eutectic High Entropy Alloys Ultra Ductile, Nat. Commun. 13 (2022) 4697. https://doi.org/10.1038/s41467-022-32444-4.

[46] Q.F. Wu, Z.J. Wang, T. Zheng, D. Chen, Z.S. Yang, J.J. Li, J.J. Kai and J.C. Wang, A Casting Eutectic High Entropy Alloy with Superior Strength Ductility Combination, Mater. Lett. 253 (2019) 268-271. https://doi.org/10.1016/j.matlet.2019.06.067.

[47] Y.S. Sato and H. Kokawa, Preferential Precipitation Site of Sigma Phase in Duplex Stainless Steel Weld Metal, Scr. Mater. 40 (1999) 659-663. https://doi.org/10.1016/s1359-6462(98)00483-7.

[48] S. Wang, Y. Li, D. Zhang, Y. Yang, S.M. Manladan and Z. Luo, Microstructure and Mechanical Properties of High Strength $AlCoCrFeNi_{2.1}$ Eutectic High Entropy Alloy Prepared by Selective Laser Melting (SLM), Mater. Lett. 310 (2022) 131511. https://doi.org/10.1016/j.matlet.2021.131511.

[49] T. DebRoy, T. Mukherjee, H.L. Wei, J.W. Elmer and J.O. Milewski, Metallurgy, Mechanistic Models and Machine Learning in Metal Printing, Nat. Rev. Mater. 6 (2021) 48-68. https://doi.org/10.1038/s41578-020-00236-1.

[50] J. Ren, M. Wu, C.Y. Li, S. Guan, J.Q. Dong, J.-B. Forien, T. Li, K.S. Shanks, D.J. Yu, Y. Chen, K. An, K.Y. Xie, W. Chen, T. Voisin and W. Chen, Deformation Mechanisms in an Additively Manufactured Dual Phase Eutectic High-Entropy Alloy, Acta Mater. 257 (2023) 119179. https://doi.org/https://doi.org/10.1016/j.actamat.2023.119179.

[51] Y.C. Zhu, S.C. Zhou, Z.P. Xiong, Y.J. Liang, Y.F. Xue and L. Wang, Enabling Stronger Eutectic High-Entropy Alloys with Larger Ductility by 3D Printed Directional Lamellae, Addit. Manuf. 39 (2021) 101901. https://doi.org/10.1016/j.addma.2021.101901.

[52] X. Jin, Y. Zhou, L. Zhang, X.Y. Du and B.S. Li, A New Pseudo Binary Strategy to Design Eutectic High Entropy Alloys Using Mixing Enthalpy and Valence Electron Concentration, Mater. Des. 143 (2018) 49-55. https://doi.org/10.1016/j.matdes.2018.01.057.

[53] Y.P. Lu, H. Jiang, S. Guo, T.M. Wang, Z.Q. Cao and T.J. Li, A New Strategy to Design Eutectic High-Entropy Alloys Using Mixing Enthalpy, Intermetallics. 91 (2017) 124-128. https://doi.org/https://doi.org/10.1016/j.intermet.2017.09.001.

[54] A. Takeuchi and A. Inoue, Classification of Bulk Metallic Glasses by Atomic Size Difference, Heat of Mixing and Period of Constituent Elements and Its Application to Characterization of the Main Alloying Element, Mater. Trans. 46 (2005) 2817-2829. https://doi.org/10.2320/matertrans.46.2817.

[55] J.X. Hou, B.X. Cao, B. Xiao, Z.B. Jiao and T. Yang, Compositionally Complex Coherent Precipitation-Strengthened High-Entropy Alloys: A Critical Review, Rare Metals. 41 (2022) 2002-2015. https://doi.org/10.1007/s12598-021-01953-4.

[56] C.J. Tong, Y.L. Chen, J.W. Yeh, S.J. Lin, S.K. Chen, T.T. Shun, C.H. Tsau and S.Y. Chang, Microstructure Characterization of $Al_xCoCrCuFeNi$ High-Entropy Alloy System with Multiprincipal Elements, Metall. Mater. Trans. A. 36 (2005) 881-893. https://doi.org/10.1007/s11661-005-0283-0.

[57] J. Ren, Y. Zhang, D.X. Zhao, Y. Chen, S. Guan, Y.F. Liu, L. Liu, S.Y. Peng, F.Y. Kong, J.D. Poplawsky, G.H. Gao, T. Voisin, K. An, Y.M. Wang, K.Y. Xie, T. Zhu and W. Chen, Strong Yet Ductile Nanolamellar High Entropy Alloys by Additive Manufacturing, Nature. 608 (2022) 62-68. https://doi.org/10.1038/s41586-022-04914-8.

[58] A. Misra, J.P. Hirth and R.G. Hoagland, Length-Scale-Dependent Deformation Mechanisms in Incoherent Metallic Multilayered Composites, Acta Mater. 53 (2005) 4817-4824. https://doi.org/10.1016/j.actamat.2005.06.025.

[59] J.J. Li, D. Ouyang, J.K. Li, M.Z. Dang, Q.H. Wang, M. Wang, C. Cai and Q.S. Wei, New Insight into the Strengthening Mechanism of $AlCoCrFeNi_{2.1}$ Eutectic High-Entropy Alloy with Dual-phase Nanolamellar Structures Achieved via Laser Powder Bed Fusion, Mater. Sci. Eng.: A. 887 (2023) 145784. https://doi.org/10.1016/j.msea.2023.145784.

[60] J.E. Bailey and P.B. Hirsch, The Dislocation Distribution, Flow Stress, and Stored Energy in Cold-Worked Polycrystalline Silver, Philos. Mag. 5 (1960) 485-497. https://doi.org/10.1080/14786436008238300.

[61] R.E. Stoller and S.J. Zinkle, On the Relationship between Uniaxial Yield Strength and Resolved Shear Stress in Polycrystalline Materials, J. Nucl. Mater. 283-287 (2000) 349-352. https://doi.org/10.1016/S0022-3115(00)00378-0.

[62] S.I. Baik, S.Y. Wang, P.K. Liaw and D.C. Dunand, Increasing the Creep Resistance of Fe-Ni-Al-Cr Superalloys via Ti Additions by Optimizing the $B2/L2_1$ ratio in Composite Nano-Precipitates, Acta Mater. 157 (2018) 142-154. https://doi.org/10.1016/j.actamat.2018.07.025.

[63] J.Y. He, H. Wang, H.L. Huang, X.D. Xu, M.W. Chen, Y. Wu, X.J. Liu, T.G. Nieh, K. An and Z.P. Lu, A Precipitation-Hardened High-Entropy Alloy with Outstanding Tensile Properties, Acta Mater. 102 (2016) 187-196. https://doi.org/10.1016/j.actamat.2015.08.076.

[64] X.D. Zhang, N. Hansen, A. Godfrey and X.X. Huang, Dislocation-Based Plasticity and Strengthening Mechanisms in Sub 20 nm Lamellar Structures in Pearlitic Steel Wire, Acta Mater. 114 (2016) 176-183. https://doi.org/10.1016/j.actamat.2016.04.040.

[65] H.Y. Yasuda, K. Shigeno and T. Nagase, Dynamic Strain Aging of $Al_{0.3}$CoCrFeNi High Entropy Alloy Single Crystals, Scr. Mater. 108 (2015) 80-83. https://doi.org/10.1016/j.scriptamat.2015.06.022.

[66] S.C. Luo, Y. Su and Z.M. Wang, Tailored Microstructures and Strengthening Mechanisms in an Additively Manufactured Dual-Phase High-Entropy Alloy via Selective Laser Melting, Sci. China Mater. 63 (2020) 1279-1290. https://doi.org/10.1007/s40843-020-1291-9.

[67] M. Calcagnotto, D. Ponge, E. Demir and D. Raabe, Orientation Gradients and Geometrically Necessary Dislocations in Ultrafine Grained Dual-Phase Steels Studied by 2D and 3D EBSD, Mater. Sci. Eng.: A. 527 (2010) 2738-2746. https://doi.org/10.1016/j.msea.2010.01.004.

[68] Z.Q. Fu, L. Jiang, J.L. Wardini, B.E. MacDonald, H.M. Wen, W. Xiong, D.L. Zhang, Y.Z. Zhou, T.J. Rupert, W.P. Chen and E.J. Lavernia, A High-Entropy Alloy with Hierarchical Nanoprecipitates and Ultrahigh Strength, Sci. Adv. 4 (2018) 8712. https://doi.org/10.1126/sciadv.aat8712.

[69] I.V. Kireeva, Y.I. Chumlyakov, Z.V. Pobedennaya and A.V. Vyrodova, Effect of γ′-phase Particles on the Orientation and Temperature Dependence of the Mechanical Behaviour of $Al_{0.3}$CoCrFeNi High-Entropy Alloy Single Crystals, Mater. Sci. Eng.: A. 772 (2020) 138772. https://doi.org/10.1016/j.msea.2019.138772.

[70] J.S. Wang, Dislocation Nucleation and the Intrinsic Fracture Behavior of $L1_2$ Intermetallic Alloys, Acta Mater. 46 (1998) 2663-2674. https://doi.org/10.1016/S1359-6454(97)00468-0.

[71] A.J. Ardell, Precipitation Hardening, Metall. Mater. Trans. A. 16 (1985) 2131-2165. https://doi.org/10.1007/BF02670416.

[72] B. Gwalani, V. Soni, M. Lee, S.A. Mantri, Y. Ren and R. Banerjee, Optimizing the Coupled Effects of Hall-Petch and Precipitation Strengthening in a $Al_{0.3}$CoCrFeNi High Entropy Alloy, Mater. Des. 121 (2017) 254-260. https://doi.org/10.1016/j.matdes.2017.02.072.

[73] S.C. Luo, C.Y. Zhao, Y. Su, Q. Liu and Z.M. Wang, Selective Laser Melting of Dual Phase $AlCrCuFeNi_x$ High Entropy Alloys: Formability, Heterogeneous Microstructures and Deformation Mechanisms, Addit. Manuf. 31 (2020) 100925. https://doi.org/10.1016/j.addma.2019.100925.

[74] E. Ma and T. Zhu, Towards Strength–Ductility Synergy Through the Design of Heterogeneous Nanostructures in Metals, Mater. Today. 20 (2017) 323-331. https://doi.org/https://doi.org/10.1016/j.mattod.2017.02.003.

[75] P.D. Niu, R.D. Li, K.F. Gan, Z.Q. Fan, T.C. Yuan and C.J. Han, Manipulating Stacking Fault Energy to Achieve Crack Inhibition and Superior Strength–Ductility Synergy in an Additively Manufactured High-Entropy Alloy, Adv. Mater. 36 (2024) 2310160. https://doi.org/https://doi.org/10.1002/adma.202310160.

[76] X.L. Wu and Y.T. Zhu, Heterogeneous Materials: a New Class of Materials with Unprecedented Mechanical Properties, Mater. Res. Lett. 5 (2017) 527-532. https://doi.org/10.1080/21663831.2017.1343208.